WITec
focus innovations

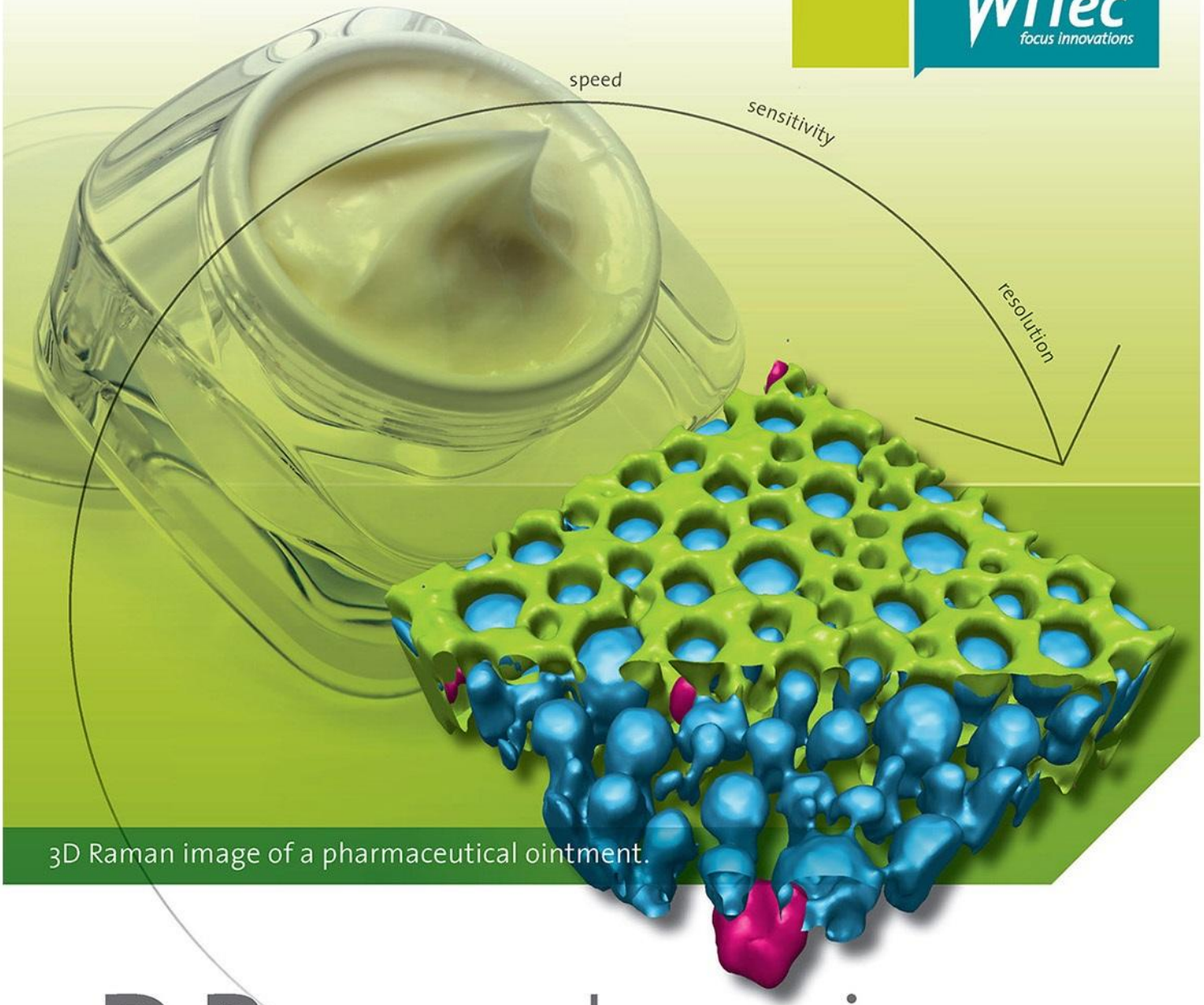

3D Raman image of a pharmaceutical ointment.

3D Raman Imaging

Turn ideas into **discoveries**

Let your discoveries lead the scientific future. Like no other system, WITec's confocal 3D Raman microscopes allow for cutting-edge chemical imaging and correlative microscopy with AFM, SNOM, SEM or Profilometry. Discuss your ideas with us at **info@witec.de.**

Raman · AFM · SNOM · RISE

www.witec.de

MADE IN **GERMANY**

Received: 10 January 2019 | Revised: 18 February 2019 | Accepted: 3 March 2019

DOI: 10.1002/jrs.5601

RESEARCH ARTICLE

WILEY Journal of RAMAN SPECTROSCOPY

Combined microfluidics–confocal Raman microscopy platform for studying enhanced oil recovery mechanisms

Jun Gao[1] | Sachin Nair[1] | Michel H.G. Duits[1] | Cees Otto[2] | Frieder Mugele[1]

[1] Physics of Complex Fluids Group and MESA+ Institute, University of Twente, Enschede, The Netherlands

[2] Medical Cell BioPhysics Group and MIRA Institute, University of Twente, Enschede, The Netherlands

Correspondence
Jun Gao, Physics of Complex Fluids Group and MESA+ Institute, University of Twente, PO Box 217, 7500AE Enschede, The Netherlands.
Email: jun.gao@utwente.nl

Funding information
Netherlands Organization for Scientific Research, Grant/Award Number: FOM-15-0521

Abstract

To study the mechanism of enhanced oil recovery, it is important to characterize the three-dimensional spatial distribution of various chemical species, especially water and oil, and their evolution during the course of water flooding. For example, visualizing the (selective) removal of oil from clay or silica substrates by low salinity water can yield important insights. Here, we present a platform that uses a microfluidic device (to represent water flooding at the pore scale) in combination with confocal Raman microscopy. Distributions of oil, water, and minerals are resolved at submicrometer resolution upon flooding water with changing composition. Using glass and gibbsite to mimic sandstone and clay, and water containing divalent cations (Ca^{2+}), we find that oil containing a fatty acid preferentially adsorbs on the gibbsite. Removal of the divalent cations leads to release of the oil droplet. This finding is consistent with the multiple ion exchange mechanism and underlines that the presence of clay is important for low salinity enhanced oil recovery. We expect that our platform will pave the road towards systematic screening of water flood compositions in more complex systems.

KEYWORDS

confocal Raman microscopy, enhanced oil recovery, low salinity, microfluidics

1 | INTRODUCTION

The standard process of recovering of crude oil from geological reservoirs using water flooding is rather inefficient and leaves approximately 30–50% of the original oil in place behind in the reservoir.[1] Various techniques of enhanced oil recovery (EOR) are being explored, improved, and applied to enhance the recovery factor, including surfactant flooding,[2,3] polymer flooding,[4,5] low salinity water flooding (LSWF),[6–12] and various other approaches.[1] While generally being tested on the level of core floods, the microscopic mechanisms controlling the efficiency of these processes are usually poorly understood. Competing mechanisms are frequently proposed and heavily debated, often on the basis of indirect evidence and insufficient microscopic information. This situation is dissatisfying yet not surprising given the complexity of the systems that involve the very specific composition of the oils and brines, the composition and geometry of the rock, and the interplay of wetting phenomena at the solid–liquid interface with flow processes on the much larger pore scale.

One manner to improve this situation is to reduce the complexity and to develop microscopic techniques that allow for a more detailed characterization of well-defined model systems. While obviously sacrificing important aspects of the complexity of the entire system, this approach can at least provide clarity whether specific proposed microscopic mechanisms claimed to alter the interaction of oil, water, and rock do function at all. Following the principles of falsification of hypotheses, this approach allows at least to rule out those proposed mechanisms that cannot even be reproduced in idealized model systems. Such mechanisms should therefore be discarded from macroscopic models for core flood experiments or reservoir models. Recent years have seen multiple improvements of existing techniques and the development of novel ones to characterize recovery systems in more detail, including atomic force microscopy (AFM),[13–15] contact angle goniometry,[16,17] X-ray tomography,[18] zeta potential analysis,[19,20] mass spectrometry,[21] quartz crystal microbalance,[22] and optical and fluorescence microscope[23] that provide access to various complementary properties. One particularly important aspect, however, that cannot be addressed using these tools is to provide a detailed map of the distribution of chemical species and its evolution in the course of a water flooding experiment. The most obvious question is how the distribution of oil and water in a model porous medium evolves upon flushing with water containing the characteristic additives of any specific EOR method. Although fluorescent dyes may be sufficient to monitor the distribution of these phases, any such label adds an additional component to the system that may change microscopic properties such as interfacial tensions and the wettability due to interfacial adsorption. Moreover, it is frequently found that the efficiency of EOR methods also correlates with the chemical composition of the rock.[10,24] The latter is usually not amenable to fluorescent labeling. In contrast, vibrational spectroscopy offers unique access to the chemical composition of materials and is—for instance—routinely used in geosciences to characterize the chemical composition of rocks.

In the present work, we present a novel platform that combines a simple microfluidic device with confocal Raman microscopy (CRM) as sketched in Figure 1. The top surface of the microfluidic device is functionalized to mimic the chemical composition of a rock surface. The external fluidic circuitry allows to flush fluids of variable composition (oil, water, and additives) through the channel and expose the surface to these materials. CRM imaging through the transparent top wall of the device allows to record spatial maps of the chemical constituents of both the surface and the fluid with a lateral and vertical resolution in the (sub)micrometer range. We describe the techniques required to extract the distribution of oil, water, and minerals from the measured Raman intensity profiles by convoluting assumed density distribution functions with the optical resolution of our instrument. We illustrate the operation of our device and the flushing procedures for a specific model system that is designed to mimic specific aspects of the so-called multiple ion exchange (MIE) mechanism,[25] which was proposed to explain the success of LSWF in sandstone reservoirs[6–12] (see below). The experiments demonstrate the functionality of our platform, and they provide microscopic evidence for the preferential adhesion of oil to clay-like surfaces mediated by divalent cations and fatty acids mimicking polar oil components.

LSWF is a relatively environmentally friendly EOR method that does only require a reduction of the salinity of the injection water rather than any expensive additives. Depending on the specific type of oil and rock, the recovery factor has been found to be enhanced anywhere between zero and around 40% for sandstone reservoirs.[10] A wide variety of possible microscopic mechanism has been proposed to explain the origin of LSWF,[8–12] including pH increase,[7] fines migration,[26,27] wettability

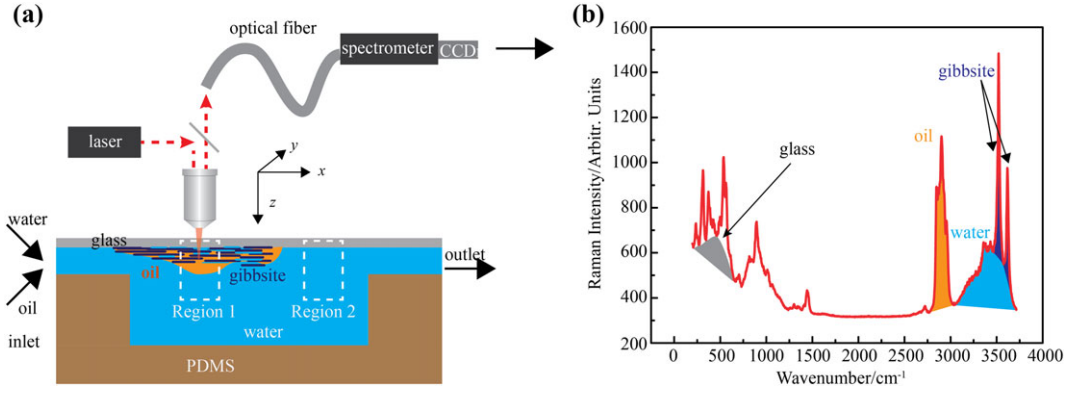

FIGURE 1 Experimental setup (a) and representative Raman spectra (b). Shaded areas in (b) are integrated bands for Raman mapping [Colour figure can be viewed at wileyonlinelibrary.com]

alteration,[12] double layer expansion,[28] and MIE.[25] The original idea of the MIE mechanism is that divalent cations present in the formation brine (primarily Ca^{2+} and/or the injection water) act as a glue to mediate binding of negatively charged acidic groups of polar oil components to negatively charged surface sites on the rock surface, such as deprotonated silanol or aluminol groups.[25] Adhering polar oil components effectively hydrophobize the intrinsically hydrophilic rock surface and thereby reduce the oil contact angle and ultimately increase the recovery factor. Flushing the reservoir with low salinity water that is in particular devoid of divalent cations would destabilize the bond between rock and polar oil components. This is supposed to induce partial desorption of the latter and make the rock somewhat more water wet, which would lead to improved recovery. Extensive tests with model systems indeed confirmed many aspects of this scenario. AFM and ellipsometric imaging of Langmuir–Blodgett layers of fatty acids showed that the stability of such layers upon exposure to water is indeed controlled by the presence of divalent cations and that the water contact angle is substantially reduced upon their removal.[13] Experiments with brine drops of variable salt content and pH wetting mica surfaces in ambient decane with dissolved fatty acids confirmed this result: Divalent cations in combination with deprotonated carboxyl groups give rise to high water contact angles due to the spontaneous formation of self-assembled Ca–stearatesurfaces, whereas complete water wetting is observed in the absence of divalent cations (and at low pH).[14] Detailed molecular dynamics simulations confirmed the strong Ca-mediated binding of deprotonated carboxyl groups to mica surfaces.[29] Subsequent macroscopic adsorption studies using the quartz crystal microbalance confirmed these trends and specifically highlighted the preferential adsorption of fatty acids (hexanoate) to gibbsite in the presence of Ca^{2+}. (The latter may sound surprising at first glance given the positive intrinsic surface charge of gibbsite. Yet an earlier detailed AFM and density functional theory simulation study showed that Ca^{2+} strongly adsorbs to gibbsite by a mechanism that is driven by hydration forces rather than electrostatics.[15]) Subsequent studies using multicomponent brines and elevated temperatures demonstrated a much more complex adsorption behavior and contact angle.[16,30] Nevertheless, the simple model system of gibbsite nanoparticles adsorbed onto silica surfaces in combination with fatty acids as model polar oil component provides an excellent and well-characterized model system to demonstrate the functionality of the combined microfluidics–CRM platform that we developed for the present study. The materials and procedures described in the following were chosen according to the specific requirements of this model system. We stress, however, that the technology platform as such is not limited to this specific application.

2 | MATERIALS AND METHODS

2.1 | Gibbsite nanoplatelets

Gibbsite nanoplatelets were synthesized using the so-called hydrothermal method, which was reported before.[31] Briefly, 0.05-M HCl was dissolved in a 0.16-M aluminum *sec*-butoxide (Sigma) aqueous solution. Then the solution was vigorously stirred for 18 hr at room temperature in a sealed container. Afterwards, it was stirred for 5 hr at 55°C, followed by heating at 180°C for 72 hr without stirring. Before use, gibbsite nanoplatelets were purified by centrifugation for 3 times at 10,000 *g* and a duration time of 30 min for each run.

For characterization purposes, the suspension was diluted 10 times, deposited on a silicon wafer, followed by rinsing with water. Subsequent AFM imaging showed that trace amounts of individual gibbsite platelets were onto a silicon wafer. AFM measurements (Dimension Icon; Bruker) reveal a characteristic lateral size of around 200 nm and a thickness of around 8 nm (see Figure S1), implying that individual gibbsite particles cannot be visualized directly by confocal Raman imaging. The size of the gibbsite particles also implies that the pore size of the gibbsite porous network will be at most 200 nm in case of a random stacking and much smaller of the order of 10 nm in case of a more or less ordered adsorption parallel to the interface. Scanning electron microscope imaging suggests a laminar configuration (Figure S2).

2.2 | Preparation of the microfluidic device

A microfluidic channel with a length of 1 cm, a width and depth of 400 μm, was fabricated from PDMS with a standard soft lithography technique using SU-8 negative resist layer as a mold, as described, for example, in our previous reports.[32] Inlet and outlet holes for the external fluidic tubing were punched with sharp tips. Glass (borosilicate) coverslips with a thickness of 170 μm are used as top wall of the channel. Simultaneously, it acts as a substrate for the oil to interact with. Chemically, the glass largely consists of silicon oxide, which—in the form of quartz—is one of the key components of typical sandstone reservoirs. The other component, which has been reported to be relevant for the success of LSWF, is clays, in particular kaolinite.[10,24] Like various other clays, kaolinite is an alumino-silicate mineral containing next to tetrahedrally

coordinated silica layers also sheets of octahedrally coordinated layers of alumina.[33] To mimic the latter in our system, we decorated the silica surfaces with nanoparticles of gibbsite (γ-$Al(OH)_3$) that were allowed to adsorb onto the glass from a drying aqueous suspension. To this end, gibbsite suspension (0.12 mg/ml, Table 1) was injected into the microfluidic channel from one end until the water front came close to the other end. The suspension was stopped there and dried in an oven (at 60°C). This procedure lead to aggregates of gibbsite nanoparticles left behind by the drying liquid front, similar to the formation of a coffee stain. In this manner, the two dominating chemical constituents of sandstone reservoirs, silica and alumina, are represented in our microfluidic device.

2.3 | Oil and water flooding protocol

Once the dried deposit of gibbsite in the microchannel is formed (Step 1 in Figure S3), we carry out a flushing protocol that mimics the steps of initial aging, oil filling, and subsequent high salinity and LSWF, as sketched in Figure S3. Confocal Raman stacks were recorded at several instances during the protocol to monitor the distribution of the relevant materials.

Taking into account the crucial role of Ca^{2+} for the adsorption of fatty acids to the mineral surfaces, we first fill the channel with a 10-mM solution of $CaCl_2$ and let it rest for 15 min (Step 2 in Figure S3). This allows Ca^{2+} ions to adsorb onto the outer and internal surfaces of the gibbsite agglomerate. The $CaCl_2$ solution thus plays the role of the formation water in a real oil reservoir. Subsequently, Step 3, the aqueous solution is flushed out by ~0.5 ml (corresponding to ~300 pore volumes) of 1-mM solution of stearic acid (Sigma) in mineral oil (BioReagent, light oil, Sigma, see Table 1). Care is taken that all water is actually removed from the channel, except for possible nanoscopic layers preferentially wetting the mineral surfaces. This solution is allowed to rest in the channel for another 15 min. During this time, we expect stearic acid to adsorb to the mineral surfaces. In the spirit of the MIE scenario, we expect that this gives rise to an adhesive bond involving the preadsorbed Ca^{2+} ions. (For the purpose of the present technical note, we assume that this process works without testing it in detail.)

After this incubation phase, the oil is replaced in Step 4 by flushing a 10-mM $CaCl_2$ solution for 15 min with a flow rate of 0.5 ml/min corresponding to an average capillary number of $Ca = \mu\bar{v}/\gamma \approx 10^{-2}$–$10^{-3}$ ($\mu \approx 10^{0}$–10^{1} mPa/s is the viscosity of the mineral oil, $\gamma \approx 50$ mN/m is the oil–water interfacial tension, and $\bar{v} \approx 3$ cm/s is the average flow velocity in the channel). This flushing process corresponds to flushing approximately 20,000 pore volumes, which is much larger than in practice where at most a few tens of pore volumes are being used.[10] This ensures that a steady-state oil distribution is reached. Finally, Step 5, the $CaCl_2$ solution is displaced by a flush with deionized (DI) water for another 15 min at the same flow rate as given above. This latter step represents the LSWF step.

TABLE 1 Compositions of the materials

Material	Composition	pH
Gibbsite suspension	0.12 mg/ml (~10^{10} particles per ml)	4.8
Mineral oil (light oil)	Contains 1-mM stearic acid	—
$CaCl_2$ solution	10 mM	5.5
DI water	—	5.9

Note. DI: deionized.

2.4 | Raman imaging

Raman images were obtained with a Witec alpha-3000 confocal Raman microscope using 35 mW of 532-nm laser and using a coverslip corrected 60× objective with a numerical aperture of 0.75. The detector is a back-illuminated electron multiplying CCD (Newton DU970N-BV, with a gain of 250). The electron multiplication provides better signal/noise ratio for weak signals and enables faster scanning for stronger signals if trading partial signal/noise ratio. All Raman data shown throughout this work were processed using principal component analysis, an established de-noising algorithm[34–36] to increase the signal/noise ratio. Typically, 10 principal components were used to de-noise the raw data.

3 | RESULTS

3.1 | Water flooding on gibbsite

A typical Raman spectrum showing all the materials involved in the present work is shown in Figure 1b. The peaks from the glass substrate at wavenumbers of 1,000 cm^{-1} at below are clearly separated from the other materials. The location of the oil, water, and gibbsite bands is as indicated in the figure. To create two-dimensional Raman intensity maps from the processed data, we integrated the spectra over the characteristic bands. For water, we integrated the broad O–H stretching band between 3,010 and 3,800 cm^{-1}. This band was subtracted as a background from the two sharp O–H stretching bands of gibbsite bands around 3,524 and 3,620 cm^{-1}. The latter are integrated from 3,466 to 3,578 cm^{-1} and from 3,578 to 3,688 cm^{-1}. For oil, we

integrated the band between 2,800 and 3,010 cm^{-1}, which is characteristic for the aliphatic C–H stretching modes. A slight tail of the water stretch vibrations at high water intensity is subtracted as a baseline, which is removed by employing the adaptive iteratively reweighted penalized least squares method.[37] The remaining intensity is then integrated from 2,800 to 3,010 cm^{-1} to obtain the intensity of the oil band. Bands from the glass substrate are integrated from 200 to 648 cm^{-1}.

Figure S4 illustrates the procedure of recording 3D Raman maps by stacking 2D images in the x–y plane on top of each other. Typically, 2D Raman images were recorded by scanning 15 pixel × 15 pixel on a 15 μm × 15 μm area with an integration time of 20 ms per pixel. Twenty-eight of such images were recorded separated by a distance of 1 μm in the z direction. This corresponds to a voxel size of 1 μm^3. The total acquisition time of such a 3D maps is 2 min.

Figures 2 and 3 show two-dimensional cross sections through two such 3D data sets in the x–y and in the x–z plane, respectively. The 3D data sets were recorded in the Region 1 of Figure 3 after flushing the microfluidic channel with $CaCl_2$ solution (Step 4 of Figure S3) and after flushing with DI water (Step 5 of Figure S3). The data after the $CaCl_2$ flush are shown in the left columns of Figures 2 and 3, the data after the DI water flush in the right columns. The x–y images in Figure 2 shown correspond to the plane $z = 1$ μm close to the surface of the gibbsite layer. (A reference level $z = 0$ μm is chosen in the vicinity of the glass surface. Due to the step size of 1 μm in the z direction, the actual position of the glass surface may deviate from $z = 0$. For most of the data shown below, the exact position of the glass surface determined after deconvoluting the Raman intensity profiles was at $z = 0.6$ μm.) The x–y images display a rather homogeneous intensity level of gibbsite, indicating a flat surface on the scale of the image. In contrast, the oil band after $CaCl_2$ flooding indicates regions of higher intensity corresponding to a small oil drop sitting on top of the gibbsite layer surrounded by regions of very low oil intensity. Correspondingly, the water signal displays a reduced intensity in the region of the oil drop (Region B) and a

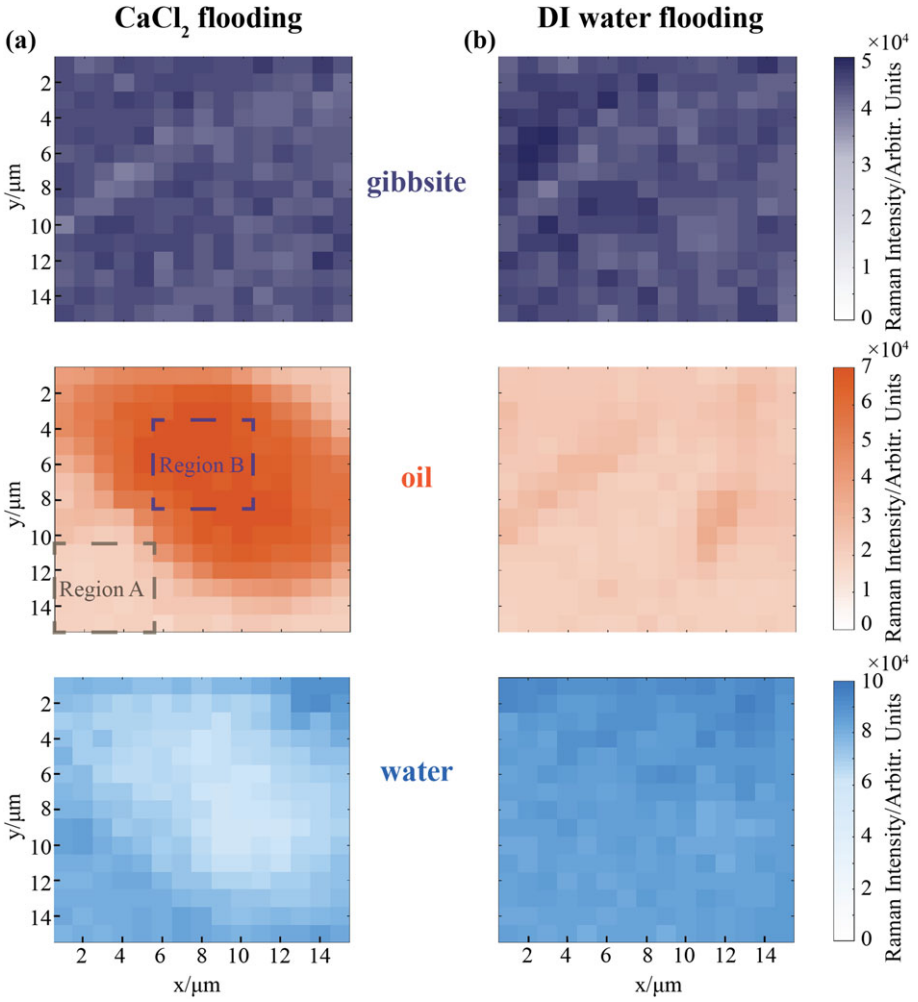

FIGURE 2 The x–y images at $z = 1$ μm in Region 1. Region 1 refers to the gibbsite covered region, as illustrated in Figure 1. DI: deionized [Colour figure can be viewed at wileyonlinelibrary.com]

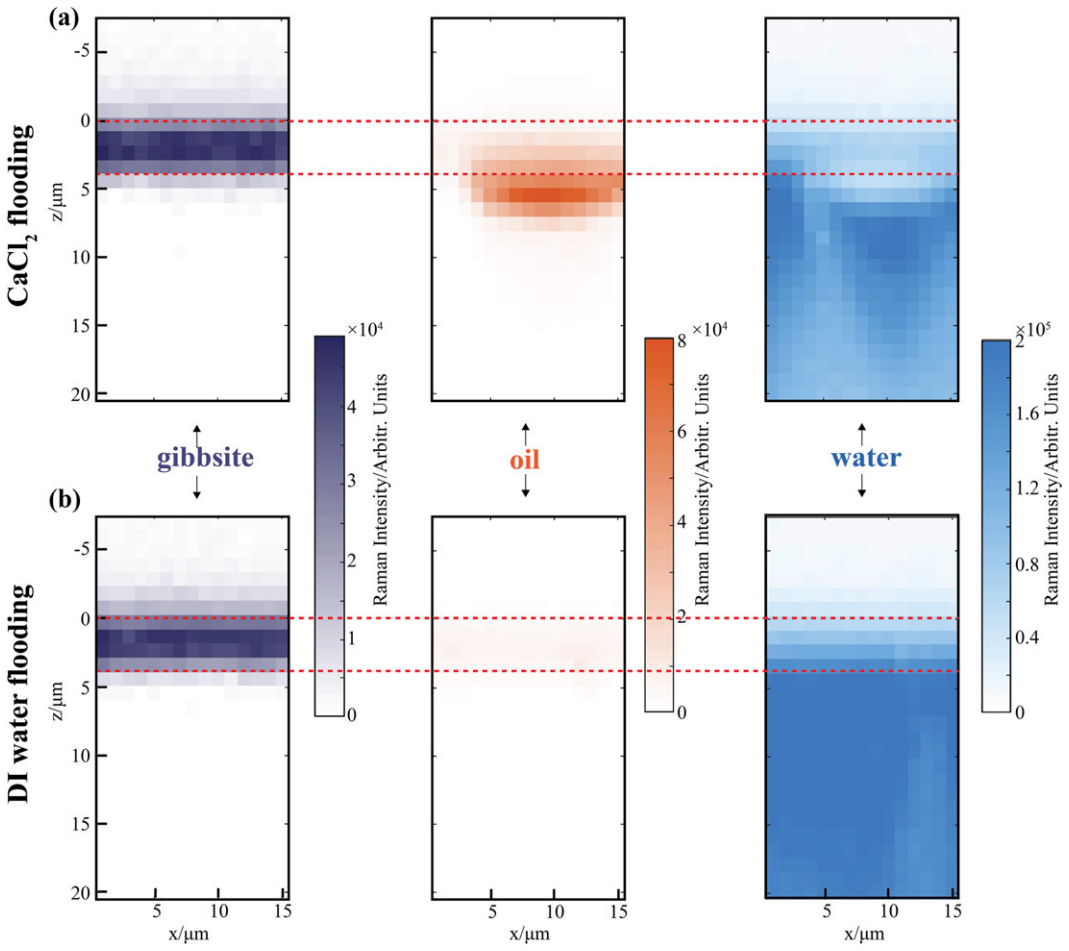

FIGURE 3 The *x*–*z* images in Region 1. Horizontal dashed red lines indicate the positions of the glass–gibbsite and the gibbsite–liquid interfaces. The intensity variations in the water signal below oil drop are attributed to refraction effect of the incident laser light at the curved oil–water interface. DI: deionized [Colour figure can be viewed at wileyonlinelibrary.com]

homogeneous intensity next to it (Region A). After flooding the channel with DI water, the oil drop has disappeared. (Figure S6 illustrates the same process for a different independent data set.)

The *x*–*z* images in Figure 3 (recorded at $y = 8$ μm) provide a vertical cross-sectional view of the same region. Again, the gibbsite layer is clearly seen in both phases of the flushing procedure indicating that the mineral deposit is stable and does not become mobilized upon flushing with DI water. That is, there is no indication of the analogue of fines migration. In contrast, the oil drop is clearly visible after the $CaCl_2$ flush but disappears after flushing with DI water. The oil is thus mobilized upon flushing with DI water. The intensity of the water band below the oil drop varies laterally. We attribute this effect to refraction due to the different refractive indices of oil and water. Moreover, it is interesting to note that a finite intensity of oil is also detected within the gibbsite layer, suggesting that this layer indeed displays pore of the nanometer scale. Although this small additional contribution is difficult to identify in Figure 3a because of the strong intensity from the oil drop, it is clearly seen in panel (b) after the DI water flush. In fact, this residual oil seems to be rather stably trapped within the gibbsite layer, as shown by the comparison of the averaged laterally intensities at the location of the drop and next to it, see Figure 4.

Figure 4 also clearly illustrates in which region the oil is replaced by water upon flushing with DI water (see arrows in panel b). Interestingly, also the water intensity profile after $CaCl_2$ flooding in Region B consists of two regions, one corresponding to the bulk water as expected and a second one representing water within the gibbsite layer, roughly at the same position as maximum of the oil intensity around $z = 2 \ldots 3$ μm.

3.2 | Water flooding on bare glass substrate

To compare the oil adsorption on gibbsite and glass, we also imaged a bare glass substrate in Region 2 in a separate experiment. Raman *x*–*z* maps of glass, oil, and water

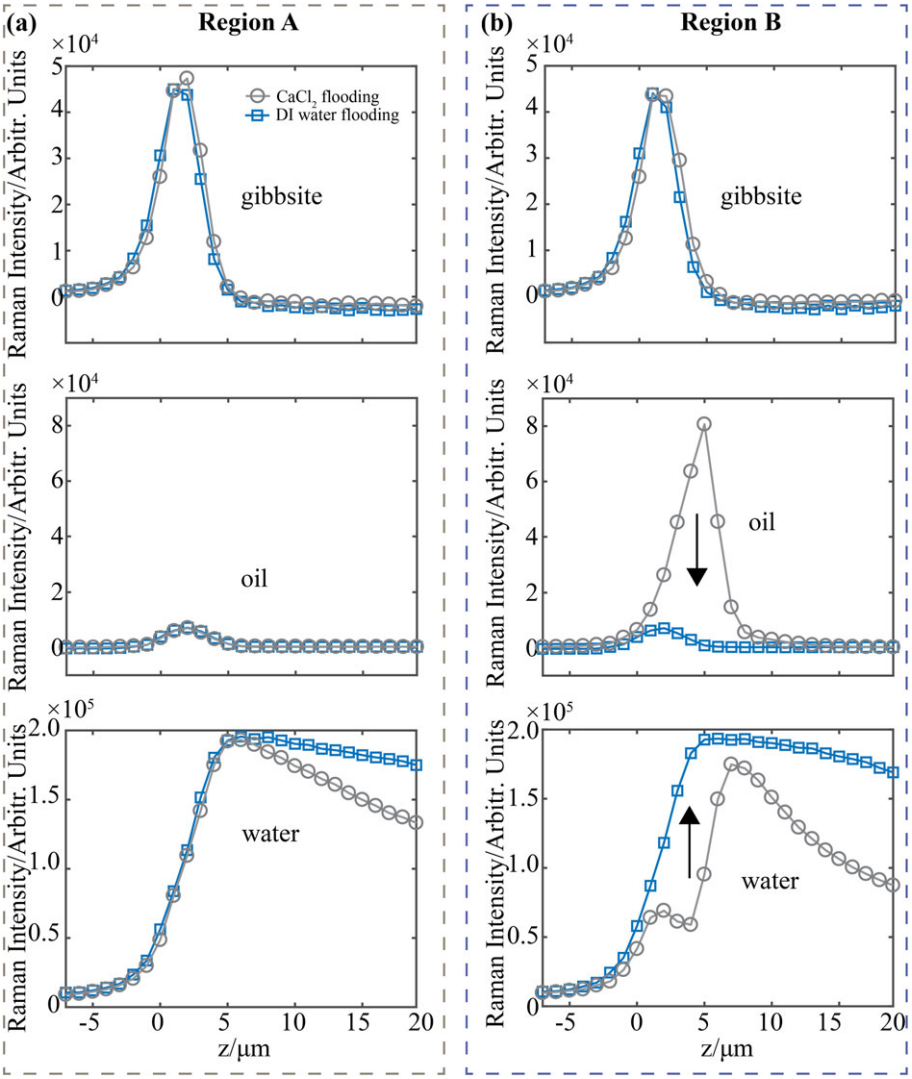

FIGURE 4 Intensity profiles along z axis. Region A refers to a region outside the oil droplet, and Region B refers to a region inside, as illustrated in Figure 2. DI: deionized [Colour figure can be viewed at wileyonlinelibrary.com]

at $y = 8$ μm are shown in Figure 5. The glass intensity remains unchanged after $CaCl_2$ and DI water flooding (Figure 5a,b), as expected. In contrast to gibbsite, however, the glass surface did not adsorb any oil, independent of the presence or absence of $CaCl_2$. Similarly, the intensity of water also did not show any obvious changes. The same applies to the average intensity profiles along the z axis. Comparing the distribution of oil on gibbsite and glass thus suggests that the oil preferentially adheres to gibbsite rather than to the glass. Naturally, removing the divalent cations then does not have any effect on the oil distribution on the glass.

3.3 | Material distribution

In addition to the mobilization of the oil drop, the confocal Raman data also contain detailed information about the distribution of oil and water within the gibbsite layer. As mentioned above, this layer consists of submicrometer-sized platelets with a thickness of the order of 10 nm, which seem to be filled with both oil and water, as indicated in Figure 3. At first glance, the raw seem to suggest the presence of a relatively high amount of oil within the gibbsite next to the gibbsite–oil interface. Yet it is not justified to directly assign a volume fraction of the fluids on the basis of their relative Raman intensities shown in these images. To an important extent, the uncertainty arises from the finite depth resolution of the confocal microscope, which implies that the measured intensity in a given plane actually arises from a sheet with a thickness of the order of 1–2 μm, given by the focal depth of the microscope. This is also the reason why the interface between the glass and the gibbsite in Region 1 and the interface between glass and water in Region 2 (see Figure 5) appear as a smooth transitions,

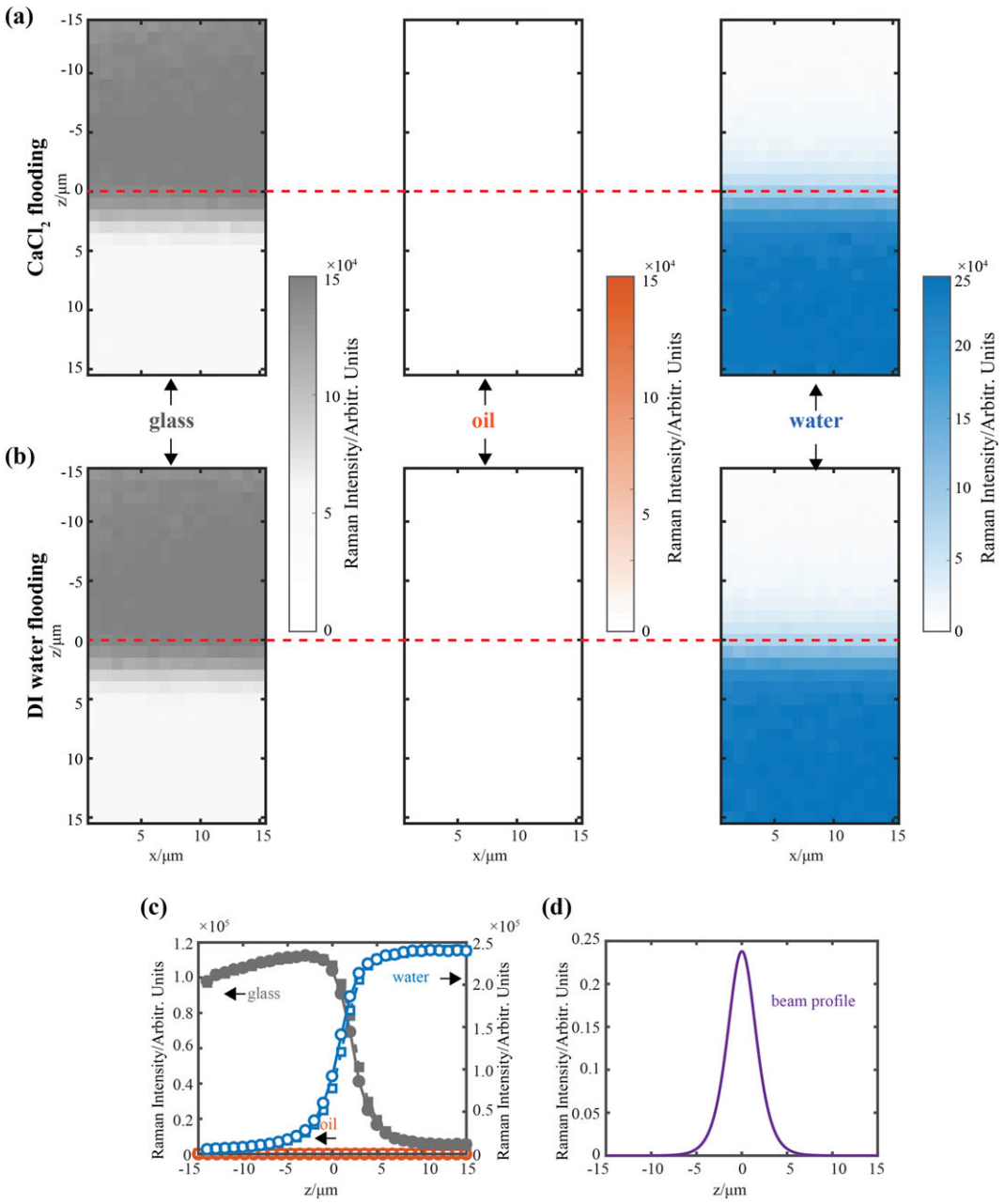

FIGURE 5 Water flooding on bare glass substrate. (a and b) The *x*–*z* images. (c) Average intensity along *z* axis. For (c), dashed line with squares represents deionized (DI) water flooding, and solid lines with circles represent $CaCl_2$ flooding. (d) Calculated beam profile [Colour figure can be viewed at wileyonlinelibrary.com]

whereas they are both sharp on the nanometer scale. Neglecting possible corrections due to reflections at various interfaces, the measured Raman intensity profile $i(z)$ results from a convolution of the Raman scattering density profile $f_j(z)$ of material j with the incident intensity profile $h(z)$:

$$i_j(z) = \int_{-\infty}^{+\infty} f_j(Z)\, h(z - Z)\, dZ. \quad (1)$$

In the simplest case, we will assume that $f_j(z)$ is simply proportional to the fraction $\rho_j(z)$ of the material in the confocal volume. To extract the actual distribution of the materials, we therefore first need to deconvolute the measured Raman intensities with the incident beam profile. Technical details of the procedure are described in the Supporting Information.

Having determined the beam profile, we extract the actual material distribution in real space by assuming rectangular boxes as distribution functions for each material. The boxes have variable positions, widths, and intensity that are used as fit parameters. For gibbsite, we assume a single layer on top of the glass substrate. Oil and water distributions are modeled with two rectangular box, one inside gibbsite accounting for the finite

penetration into the porous layer and one outside to describe the bulk material (Figure 6). From Equation (1), we then optimize the fit parameters to reproduce the measured intensity profiles $i(z)$ in Figure 6.

The deconvoluted results in Figure 6 show that gibbsite layer in the present experiment had a thickness of 2.0 μm. Water penetrated into gibbsite layer all the way down to the substrate, whereas oil penetration was limited to the top 1.4 μm and did not reach the glass substrate. The oil within the gibbsite layer seems to be trapped stably, independent of whether the channel is flushed with $CaCl_2$ solution or DI water.

The oil drop in Region B after $CaCl_2$ flooding is found to have a thickness of 2.2 μm on top of the gibbsite layer. Inside the gibbsite layer, there is the same amount of oil adsorbed as next to the drop. After flushing with DI water, the 2.2-μm-thick oil droplet is removed and replaced with the same thickness of water. On the basis of these results, we conclude that the nanopores in between the gibbsite platelets are partially filled with oil and water. This entrapped fluid is rather stable for the conditions of the present experiment; no exchange of these fluids is observed. In contrast, additional oil adsorbed in the form of a drop on the gibbsite in the presence of Ca is removed upon flushing with DI water. In contrast, on the flat glass surface next to the gibbsite, we do not find any stably anchored oil drops under Ca flushing conditions. This scenario is summarized schematically in Figure 7.

4 | DISCUSSIONS

The experimental observations described above illustrate the possibilities of our combined confocal Raman–microfluidics platform for studying in situ the relative

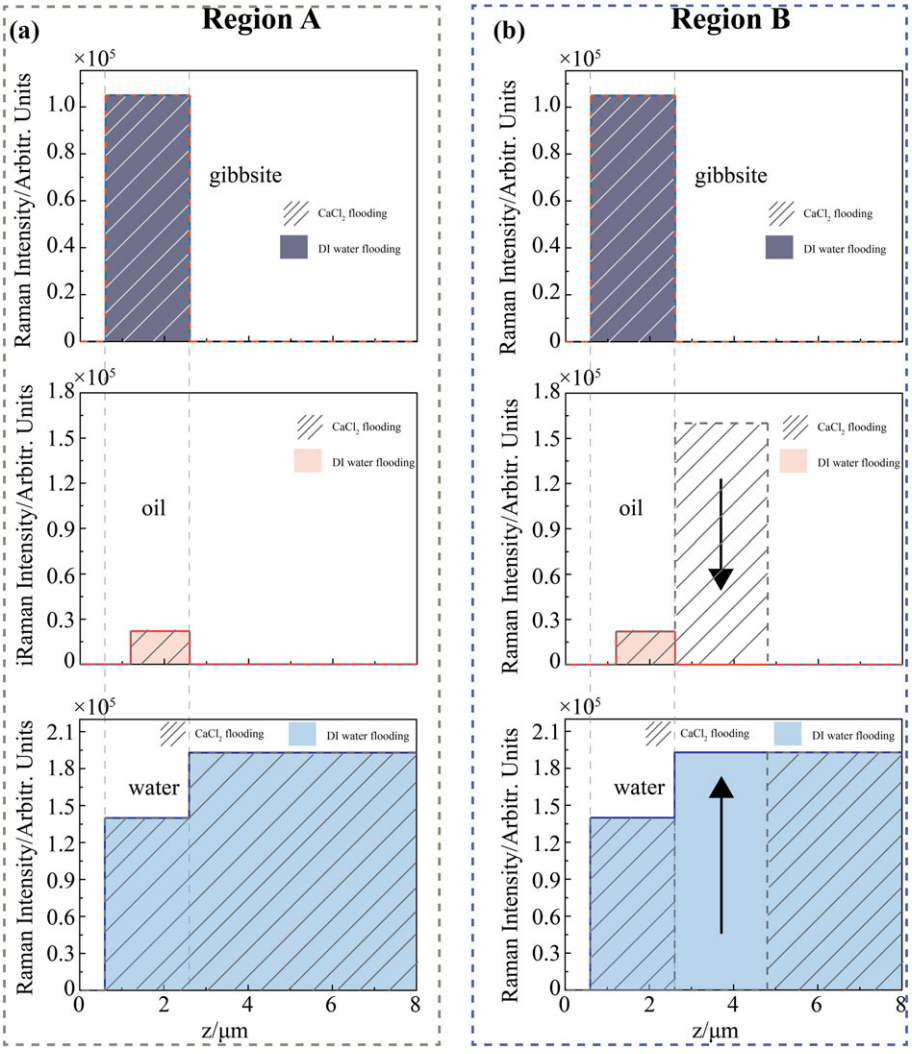

FIGURE 6 Deconvoluted distribution profiles. Arrows indicate variations of oil and water distribution upon exchanging $CaCl_2$ solution with deionized (DI) water. Region A refers to a region outside the oil droplet, and Region B refers to a region inside, as illustrated in Figure 2 [Colour figure can be viewed at wileyonlinelibrary.com]

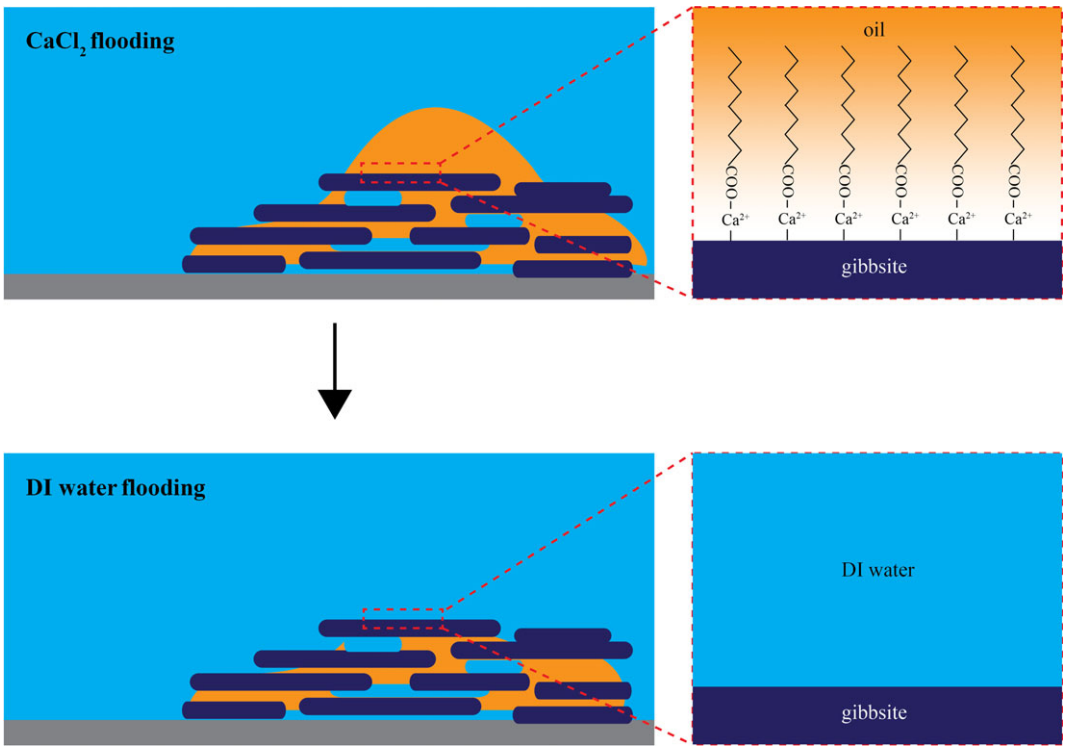

FIGURE 7 Schematic illustration of the oil–water–gibbsite distribution and oil removal. Zoomed view: suspected microscopic binding mechanism consistent with Wang et al.[22] DI: deionized [Colour figure can be viewed at wileyonlinelibrary.com]

distribution of oil, water, and minerals in two-phase flow system with chemically and topographically heterogeneous walls. From an applied perspective, the model system and the limited set of conditions in the present system were chosen to verify specific aspects of the MIE mechanism[25] proposed to explain the success of LSWF. The results provide microscopic illustration of the macroscopic observation that the presence of aluminum hydroxides (naturally, e.g., in the form of kaolinite) in reservoir rocks is favorable for successful LSWF.[10,24] The fact that the oil preferentially sticks to the gibbsite (rather than the neighboring SiO2) suggests this idea. The observation is also consistent with a series of microscopic and macroscopic experiments in our laboratory, in which we demonstrated that divalent cations bind strongly to minerals such as gibbsite[15] and kaolinite[38] and enhance the binding of fatty acids to these surfaces,[22] presumably by forming in bridges, as sketched in Figure 7. On a macroscopic scale, this effect has been shown to render surfaces more oil wetting, and it was also demonstrated that removing the Ca ions from the solution reverts the system again towards more water wetting.[13,14] By monitoring the adhesion and subsequent removal of oil drops on the micrometer scale, the present experiments provide the thus far missing link between the atomic scale ion adsorption and surface charge studies and macroscopic wettability alteration. They demonstrate that the fatty acid layers that are adsorbed via Ca^{2+}-mediated bonding indeed act as anchors that mediate the binding of oil to the clay fraction of the mineral surface. Obviously, more extensive experiments will be required to test the generality of the observations for variable degrees of complexity of the system, including fluid composition, surface heterogeneities, and variable temperature.

Technically, the lateral and spectroscopic resolution will allow to discern different chemical species with a lateral and depth resolution on the order of 1 μm. Variations of the topography such as the oil drop seen in the present experiment pose certain challenges because they refract the incident light, as discussed in the context of Figure 3. The resulting variations of the Raman intensity compromise the fitting procedure to extract the material distribution shown in Figure 6. More advanced fitting strategies will be required to better quantify the relative fraction of material within the confocal volume.

In future studies, it will be interesting to apply the platform to more complex systems that approached the real EOR more closely, for example, a system having heterogeneous distribution of quartz and clay, different compositions of water, oil, and mineral substrates, different flooding velocity, high temperature, and high pressure. These complexities can be studied individually with our platform to underpin the effect of each. Preliminary experiments suggest that the strong fluorescence background of some natural clays or oil and the strongly

overlapped Raman peaks of organic materials will pose challenges that need to be overcome using advanced background subtraction tools.[37]

5 | CONCLUSIONS

In this work, we demonstrated a platform combining 3D confocal Raman imaging and a simple microfluidic channel to study specific aspects of the chemical interaction of carboxylates, divalent cations, and mineral surfaces in the context of EOR. We demonstrated that Ca^{2+} ions dissolved in the aqueous phase in combination with stearic acid dissolved in the oil phase can give rise to preferential adhesion of oil in the form of micrometer-sized drops to deposits of aluminum hydroxide (gibbsite) on a silica surface. Upon flushing reducing the Ca^{2+} concentration by flushing with pure water, these drops are mobilized. CRM enables a unique characterization of the distribution of these materials on the submicrometer scale. Interestingly, the results also suggest a partial penetration of both water and oil into the nanoporous deposits of gibbsite. We expect that future investigations of 3D confocal Raman imaging combined with microfluidics will enable a much more detailed characterization of the microscopic chemical effects that control the efficiency of various EOR methods.

ACKNOWLEDGEMENTS

This work is a part of an Industrial Partnership Program of the Netherlands Organization for Scientific Research (NWO) through FOM Concept agreement FOM-15-0521. Financial support was provided through the Exploratory Research (ExploRe) programme of BP plc. BP Exploration Operating Company Limited are thanked for permission to publish this paper. The authors thank Dr. H.T.M. van den Ende for helpful discussion on the Raman profile deconvolution.

ORCID

Jun Gao https://orcid.org/0000-0003-2106-3134

REFERENCES

[1] A. Muggeridge, A. Cockin, K. Webb, H. Frampton, I. Collins, T. Moulds, P. Salino, *Philos. Trans. Royal Soc. A* **2014**, *372*, 25.

[2] G. Hirasaki, C. A. Miller, M. Puerto, *SPE J.* **2011**, *16*, 889.

[3] H. J. Hill, J. Reisberg, G. L. Stegemeier, *J. Pet. Technol.* **1973**, *25*, 186.

[4] J. J. Sheng, B. Leonhardt, N. Azri, *J. Can. Pet. Technol.* **2015**, *54*, 116.

[5] R. B. Needham, P. H. Doe, *J. Pet. Technol.* **1987**, *39*, 1503.

[6] K. J. Webb, C. J. J. Black, H. Al-Ajeel, *Middle East Oil Show*, Society of Petroleum Engineers, Bahrain **2003**.

[7] P. L. McGuire, J. R. Chatham, F. K. Paskvan, D. M. Sommer, F. H. Carini, *SPE Western Regional Meeting*, Society of Petroleum Engineers, Irvine **2005**.

[8] J. J. Sheng, *J. Pet. Sci. Technol.* **2014**, *120*, 216.

[9] E. W. Al-Shalabi, K. Sepehrnoori, *J. Pet. Sci. Technol.* **2016**, *139*, 137.

[10] M. D. Jackson, J. Vinogradov, G. Hamon, M. Chamerois, *Fuel* **2016**, *185*, 772.

[11] S. Strand, T. Puntervold, T. Austad, *J. Pet. Sci. Eng.* **2016**, *146*, 1079.

[12] P. C. Myint, A. Firoozabadi, *Curr. Opin. Colloid Interface Sci.* **2015**, *20*, 105.

[13] N. Kumar, L. Wang, I. Siretanu, M. Duits, F. Mugele, *Langmuir* **2013**, *29*, 5150.

[14] F. Mugele, B. Bera, A. Cavalli, I. Siretanu, A. Maestro, M. Duits, M. Cohen-Stuart, D. van den Ende, I. Stocker, I. Collins, *Sci. Rep.* **2015**, *5*(8).

[15] I. Siretanu, D. Ebeling, M. P. Andersson, S. L. S. Stipp, A. Philipse, M. C. Stuart, D. van den Ende, F. Mugele, *Sci. Rep.* **2014**, *4*, 7.

[16] M. E. J. Haagh, I. Siretanu, M. H. G. Duits, F. Mugele, *Langmuir* **2017**, *33*, 3349.

[17] B. Bera, M. H. G. Duits, M. A. C. Stuart, D. van den Ende, F. Mugele, *Soft Matter* **2016**, *12*, 4562.

[18] J. Murison, B. Semin, J.-C. Baret, S. Herminghaus, M. Schröter, M. Brinkmann, *Phys. Rev. Appl.* **2014**, *2*, 034002.

[19] J. Yang, Z. X. Dong, M. Z. Dong, Z. H. Yang, M. Q. Lin, J. Zhang, C. Chen, *Energy Fuels* **2016**, *30*, 72.

[20] A. Alroudhan, J. Vinogradov, M. D. Jackson, *Colloids Surf., A* **2016**, *493*, 83.

[21] I. R. Collins, J. W. Couves, M. Hodges, E. K. McBride, C. S. Pedersen, P. A. Salino, K. J. Webb, C. Wicking, H. Zeng, *SPE Improved Oil Recovery Conference*, Society of Petroleum Engineers, Tulsa **2018**.

[22] L. Wang, I. Siretanu, M. H. G. Duits, M. A. C. Stuart, F. Mugele, *Colloids Surf., A* **2016**, *494*, 30.

[23] S. Berg, A. W. Cense, E. Jansen, K. Bakker, *Petrophysics* **2010**, *51*, 9.

[24] N. Morrow, J. Buckley, *J. Pet. Technol.* **2011**, *63*, 106.

[25] A. Lager, K. J. Webb, C. J. J. Black, M. Singleton, K. S. Sorbie, *Petrophysics* **2008**, *49*(8).

[26] G.-Q. Tang, N. R. Morrow, *J. Pet. Sci. Eng.* **1999**, *24*, 99.

[27] W. Song, A. R. Kovscek, *Lab Chip* **2015**, *15*, 3314.

[28] D. J. Ligthelm, J. Gronsveld, J. Hofman, N. Brussee, F. Marcelis, H. van der Linde, *EUROPEC/EAGE Conference and Exhibition*, Society of Petroleum Engineers, Amsterdam **2009**.

[29] K. Kobayashi, Y. Liang, S. Murata, T. Matsuoka, S. Takahashi, K. Amano, N. Nishi, T. Sakka, *J. Phys. Chem. C* **2017**, *121*, 9273.

[30] M. E. J. Haagh, N. Schilderink, M. H. G. Duits, I. Siretanu, F. Mugele, I. R. Collins, *J. Pet. Sci. Eng.* **2018**, *165*, 1040.

[31] S. Louaer, Y. Wang, L. Guo, *ACS Appl. Mater. Interfaces* **2013**, *5*, 9648.

[32] L. Wang, C. Zhao, D. Wijnperlé, M. H. G. Duits, F. Mugele, *Biomicrofluid.* **2016**, *10*, 034113.

[33] G. Sposito, *The chemistry of soils*, Oxford university press, Oxford **2008**.

[34] A. de Cheveigné, J. Z. Simon, *J. Neurosci. Methods* **2007**, *165*, 297.

[35] D. Balvay, N. Kachenoura, S. Espinoza, I. Thomassin-Naggara, L. S. Fournier, O. Clement, C.-A. Cuenod, *Radiology* **2011**, *258*, 435.

[36] B. M. Liszka, H. S. Rho, Y. Yang, A. T. M. Lenferink, L. Terstappen, C. Otto, *Rsc Adv.* **2015**, *5*, 49350.

[37] Z. Zhang, S. Chen, Y. Liang, *Analyst* **2010**, *135*, 1138.

[38] N. Kumar, C. L. Zhao, A. Klaassen, D. van den Ende, F. Mugele, I. Siretanu, *Geochim. Cosmochim. Acta* **2016**, *175*, 100.

SUPPORTING INFORMATION

Additional supporting information may be found online in the Supporting Information section at the end of the article.

How to cite this article: Gao J, Nair S, Duits MHG, Otto C, Mugele F. Combined microfluidics–confocal Raman microscopy platform for studying enhanced oil recovery mechanisms. *J Raman Spectrosc*. 2019;1–12. https://doi.org/10.1002/jrs.5601